

Genuine Ohmic van der Waals contact between indium and MoS₂

Bum-Kyu Kim^{1†}, Dong-Hwan Choi^{1,2†}, Tae-Hyung Kim^{3†}, Hanul Kim², Kenji Watanabe⁴, Takashi Taniguchi⁴, Heesuk Rho², Yong-Hoon Kim^{3*}, Ju-Jin Kim^{2*}, and Myung-Ho Bae^{1,5*}

¹Korea Research Institute of Standards and Science, Daejeon 34113, Republic of Korea

²Department of Physics, Research Institute of Physics and Chemistry, Chonbuk National University, Jeonju 54896, Republic of Korea

³School of Electrical Engineering, Korea Advanced Institute of Science and Technology, 291 Daehak-ro, Yuseong-gu, Daejeon 34141, Republic of Korea

⁴National Institute for Materials Science, 1-1 Namiki, Tsukuba 305-0044, Japan

⁵Department of Nano Science, University of Science and Technology, Daejeon, 34113, Republic of Korea

†These authors contributed equally to this work.

*e-mail: y.h.kim@kaist.ac.kr; jujinkim@chonbuk.ac.kr; mhbae@kriss.re.kr

Abstract

The formation of an ideal van der Waals (vdW) contacts at metal/transition-metal dichalcogenide (TMDC) interfaces is a critical step for the development of high-performance and energy-efficient electronic and optoelectronic applications based on the two-dimensional (2D) semiconductors. In overcoming the key challenges of the conventional metal deposition process that leads to an uncontrollable Schottky barrier height and high contact resistance, notable advances were recently made by transferring atomically flat metal thin films¹ or thermally evaporating indium/gold alloy². However, the realization of an ideal vdW contact between an elemental metal and TMDC through the evaporation process is yet to be demonstrated,

and particularly the evidence of an Ohmic contact between three-dimensional metallic electrodes and TMDCs is still unavailable. Herein, we report the fabrication of atomically clean metal/TMDC contacts by evaporating metals at a relatively low thermal energy and subsequently cooling the substrate holder down to ~ 100 K by liquid nitrogen, achieving for the indium (In)/molybdenum disulfide (MoS_2) case an accumulation-type Ohmic contact with a metal-induced electron doping density of $\sim 10^{12} \text{ cm}^{-2}$. We find that the transport at the In/ MoS_2 contact is dominated by the field-emission mechanism over a wide temperature range from 2.4 to 300 K, and the contact resistance reaches $\sim 600 \Omega \mu\text{m}$ and $\sim 1,000 \Omega \mu\text{m}$ at cryogenic temperatures for the few-layer and monolayer MoS_2 cases, respectively. Based on first-principles calculations, we find that the nature of the ideal In/ MoS_2 vdW contact is characterized by the formation of in-gap states within TMDC together with the abrupt and rigid shift of the TMDC band. Demonstrating the genuine Ohmic vdW contacts through the evaporation process, this work paves a practically available path for fabricating high-quality metal/2D semiconductor contacts for next-generation electronic and optoelectronic applications.

Layered semiconducting transition-metal dichalcogenides (TMDCs) such as MoS_2 , WSe_2 and MoTe_2 have been extensively studied for the future development of low-power and high-performance electronics and optoelectronics^{3,4,5}. In realizing two-dimensional (2D) electronic devices based on TMDCs, because each TMDC atomic layer in the bulk form is coupled with neighboring layers through van der Waals (vdW) interactions, mono- or few-layer TMDC flakes can be deposited onto a substrate via a mechanical exfoliation method³. Meanwhile, establishing a reliable

Ohmic contact across the Schottky barriers between metals and TMDCs remains a critical challenge^{6,7}. For instance, in reducing the Schottky barrier height for TMDCs, efforts to identify metals with appropriate work functions Φ_{metal} (e.g. $\Phi_{\text{Sc}} \approx 3.5$ eV for Sc and $\Phi_{\text{Ti}} \approx 4.3$ eV for Ti) based on the affinity of TMDC (e.g. monolayer MoS₂: $\chi_{1\text{L MoS}_2} \approx 4$ eV, multilayer MoS₂: $\chi_{\text{ML MoS}_2} \approx 4.3$ eV) have not been effective because of the strong Fermi-level pinning (FLP) effect^{8,9}. While various approaches have been explored to overcome this problem, including molecular doping¹⁰, tunnel-barrier insertion^{11,12}, fabrication of graphene contacts^{13,14}, and phase changes¹⁵, a recent study has shown that the formation of an ideal metal-TMDC vdW contact through the transfer of atomically flat metal thin films significantly improves the contact properties.¹ Here, it was important to recognize that the conventional thermal evaporation process of metals typically introduces crystalline defects in TMDCs and leads to an uncontrollable Schottky barrier height (or FLP) and high contact resistance^{9,1}. More recently, another breakthrough was made by introducing the thermal-evaporation process of In alloy with Au, leading to clean vdW-type contacts for single- and few-layer MoS₂ and achieving the lowest contact resistance between three-dimensional (3D) metals and 2D semiconductors². However, question still remains whether it is also possible to form an ideal vdW contact for 2D semiconductors with a single elemental metal through the evaporation process. Furthermore, if the low contact resistance through the vdW contact can be achieved, one needs to elucidate the origins, i.e., what is the nature of the charge transport and band alignment at the interface and whether the transport across the contacts is thermionic or field emission.

Here, we report the Ohmic vdW contact formed between pure In and MoS₂, and characterize the In/MoS₂ interface by the transmission electron microscope (TEM) measurement, transport measurements at varying temperature (T) and carrier density (n_e), and first-principles calculations. A key to this achievement was the relatively low-evaporation T of In at ~ 530 °C with the extremely

low T of the substrate holder at ~ 100 K in the In deposition process, which allows the preparation of an atomically clean In/MoS₂ interface. If an ideal vdW-type contact is achieved, the relatively low work function of In ($\Phi_{\text{In}} \approx 4.1$ eV) should result in a good contact resistance for MoS₂. For both single- and few-layer MoS₂ devices prepared through our approach, we indeed find that the contact resistance decreases with decreasing temperature, reaching to the record-level $1 \text{ k}\Omega \mu\text{m}$ and $0.6 \text{ k}\Omega \mu\text{m}$, respectively. This behavior indicates the Ohmic character of the In/MoS₂ contact or the field emission is the dominant charge transport mechanism at the In/MoS₂ contact. Carrying out first-principles calculations for realistic In/MoS₂ contact models, we find that the atomistic origins of the high-quality Ohmic vdW contact can be traced to the weak In/MoS₂ interactions and yet the formation of in-gap states within the contact-region MoS₂ to support the interfacial charge transport.

Preparation and characterization of van-der-Waals In/MoS₂ interface

We fabricated MoS₂ field-effect transistors (FETs) on hBN flakes, where the hBN flakes were deposited onto a 300-nm-thick SiO₂/Si substrate by mechanical exfoliation. We then transferred a few-layer MoS₂ flake (HQ-graphene, Inc.) onto a selected hBN flake^{13,16}. For the electrical measurements, we deposited 100 nm-thick In electrodes across the MoS₂ channel, where the substrate holder was kept at ~ 100 K by flowing liquid nitrogen through it (see Fig. 1a). The substrate cooling process leads to an important result; a uniform surface morphology of indium film is achieved, which contrasts strongly with the usage of a room-temperature holder that produces a segregated granular film for at least up to ~ 70 nm thickness, as reported in our previous work¹⁷. The upper panel of Fig. 1b shows a cross-sectional transmission electron microscopy (TEM) image of the In/few-layered MoS₂ junction of a separately prepared sample, which clearly shows an atomically

separated interface between In and MoS₂ layers without any metal invasion into the MoS₂ layers. Whereas crystal-lattice disorders that cause defect-induced gap states and FLP typically occur during the high-temperature deposition process of evaporated metal atoms with high thermal energy^{9,1}, the In deposited at a relatively low thermal energy could apparently provide a clean vdW interface without disorder or defect. For instance, whereas the evaporation temperature of Au at 10⁻⁷ Torr is ~860 °C, only ~530 °C is required for the evaporation of In at the same pressure. For comparison, we also prepared an Au/few-layered MoS₂ junction, where the substrate holder was also kept at ~100 K during Au deposition. The lower panel of Fig. 1b shows a TEM image of the junction having atomic defects at the first and second layers from the top of MoS₂, due to the invasion of Au atoms during deposition process.

Basic electrical properties of a few-layer MoS₂ field-effect transistor

Figure 1c shows a photograph of a MoS₂ FET on a 22 nm-thick hBN flake. The number of MoS₂ layers was estimated to be $n = 6$ (see Supplementary Fig. S1). The multiple electrodes for the six-layer (6L) MoS₂ flake with different intervals between two neighboring electrodes were designed to measure the contact resistance via the transfer-length method (TLM)¹⁵, i.e., four FETs with different channel lengths ($L_1 = 0.5 \mu\text{m}$, $L_2 = 1 \mu\text{m}$, $L_3 = 1.5 \mu\text{m}$, and $L_4 = 2 \mu\text{m}$ from the left channel in the region indicated by a dashed box). Here, the widths (W) of all channels were nearly identical at $2 \mu\text{m}$. Figure 1d shows the two-probe conductance as a function of the back-gate voltage ($G-V_G$) of the L_2 -FET with a source-drain voltage (V_{SD}) of 30 mV at various temperatures. The conductance decreased for negatively decreasing V_G and reached zero near $V_G \approx 0 \text{ V}$ throughout the investigated temperature range, which indicates that the carriers are electrons. The two-probe conductance increased with decreasing T at a given V_G for $V_G > 10 \text{ V}$, i.e., the device exhibited a

metallic behavior. However, the opposite behavior was observed near a depletion region of $0 < V_G < 10$ V, representing an insulating character. These behaviors are consistent with the current–voltage (I – V_{SD}) curves for various V_G values at $T = 2.5$ K in Supplementary Fig. S2a. For instance, the I – V_{SD} curves for $V_G > 10$ V and $0 < V_G < 10$ V show linear and nonlinear characteristics, respectively. The four-probe measurements for the L_2 channel also showed a similar V_G value for the metal–insulator crossover location (see Supplementary Fig. S2b and S2c). This result indicates that the crossover behavior is mainly determined by the transport in the MoS₂ channel, not in the contact part. In the field-effect mobility (μ) as a function of T (see Supplementary Fig. S3), the mobility showed the temperature dependence of $T^{-2.2}$ at $T > 100$ K with $\mu \approx 50$ cm²V⁻¹s⁻¹ at room temperature. This behavior is similar to the bulk MoS₂ ($\mu \propto T^{-2.5}$) with optical phonon scattering as the dominant scattering mechanism^{18,13}. When $T < 20$ K, μ became saturated at 3200 cm² V⁻¹ s⁻¹ with decreasing temperature for the four-probe measurement. The saturation behavior in the low- T regime has been known to occur when the impurity scattering plays a dominant role and the phonon effect is suppressed¹⁹.

Contact resistance at In/MoS₂ contacts

On the basis of the TLM measurements (see Supplementary Fig. S4) with multiple channels (see Fig. 1c), we extracted the contact resistance ($R_c W$) as a function of n_e of a 6L-MoS₂ device at representative temperatures; the results are shown in Fig. 2a (scattered solid squares). Here, n_e was estimated from the relation $n_e = (e\mu R_{sh})^{-1}$, where the sheet resistance R_{sh} and μ were obtained from the four-probe measurements. We note that the obtained contact resistance includes a serial resistance of In electrodes. At a given temperature, $R_c W$ decreased with increasing n_e . The contact resistance is given by^{6,7}

$$R_c W (n_e, T) = \sqrt{R_{sh}(n_e, T) \rho_c(n_e, T)}, \quad (1)$$

which is only valid for $L_c \gg L_T$. Here, L_c and $L_T (= \sqrt{\rho_c/R_{sh}})$ are respectively the contact length and transfer length, the latter of which represents the average distance that charge carriers flow in a semiconductor beneath the contact before they completely transport to the electrode. Figure S4 shows that our device satisfied this condition with $L_c \approx 1 \mu\text{m}$ and $L_T \approx 0.1 \mu\text{m}$. Equation (1) implies that $R_c W$ decreases with increasing n_e because both R_{sh} and ρ_c generally decrease with increasing n_e .

At a fixed n_e , whereas the thermionic emission charge transport mechanism across the Schottky barrier predicts that $R_c W$ increases with decreasing T because of suppression of the thermionic emission²⁰, $R_c W$ in our measurements decreased with decreasing T as shown in Fig. 2a. Figure 2b shows $R_c W$ as a function of T at $n_e = 3.4 \times 10^{12} \text{ cm}^{-2}$. The contact resistance decreased from 2.3 to 0.6 $\text{k}\Omega \mu\text{m}$ when T was decreased from room temperature to 2.4 K. This behavior has been reported in several previous works such as graphene/MoS₂¹³ and Pd/graphene contacts²¹; it is considered as an evidence for the non-dominant role of thermionic emission for the contact transport mechanism. Figure 2b also shows R_{sh} as a function of T at $n_e = 3.4 \times 10^{12} \text{ cm}^{-2}$, where R_{sh} decreased with decreasing T because the phonon scattering is reduced.

Mechanism of transport at In/MoS₂ contacts

We next examined which component between R_{sh} and ρ_c predominantly determines the contact resistance of the In/MoS₂ vdW contact. We included other reports in Fig. 2a for comparison; graphene(Gr)/four-layer (4L)-MoS₂ ($n = 4$) contact,¹³ Au/4L-MoS₂²⁰ and Au/In/few-layer MoS₂². In the case of Gr/4L-MoS₂, the graphene functions as a work-function-controllable contact material,

which leads to a lower contact resistance, i.e., $R_c W \approx 1 \text{ k}\Omega \mu\text{m}$ at $n_e > 4 \times 10^{12} \text{ cm}^{-2}$ and $T = 12 \text{ K}$ (see the red curve in Fig. 2a). Although both the Gr- and In-contact MoS₂ devices gave a similar minimum $R_c W$ at cryogenic temperatures, we conclude that the transport mechanisms at the contacts differ from each other. In the In/MoS₂ contact case, $R_c W$ decreased with decreasing T for the examined n_e range, representing the field emission (or tunneling) for all examined T and n_e ranges. However, the $R_c W$ - n_e curves obtained at $T = 12$ and 250 K for the Gr/4L-MoS₂ device suggest that the left and right sides with respect to $n_e \approx 2 \times 10^{12} \text{ cm}^{-2}$ followed the thermionic and field emissions at the contact, respectively. At $T = 12 \text{ K}$ for the Gr/4L-MoS₂ device, although the $R_c W$ of $\sim 1 \text{ k}\Omega \mu\text{m}$ was relatively insensitive to the variation of n_e in the range from 4×10^{12} to $7 \times 10^{12} \text{ cm}^{-2}$, it rapidly changed from $1 \text{ k}\Omega \mu\text{m}$ to $6 \text{ k}\Omega \mu\text{m}$ when n_e decreased from $3 \times 10^{12} \text{ cm}^{-2}$ to $1.5 \times 10^{12} \text{ cm}^{-2}$. In the case of the Au/4L-MoS₂ contact, $R_c W$ was increased with decreasing temperature, representing the thermionic emission. For the Ohmic contact case of the In/6L-MoS₂ device, on the other hand, the slopes in the $R_c W$ - n_e curves were nearly unchanged for varying temperature and $R_c W$ at a given temperature was also relatively insensitive to n_e . In this view, the slope of the Au/In/few layer-MoS₂ contact was similar to that for the thermal emission. In our In/6L-MoS₂ device (see Fig. 3a), R_{sh} varies in the range from 1 to $80 \text{ k}\Omega$ when ρ_c only varies from 5×10^{-6} to $5 \times 10^{-7} \Omega \text{ cm}^2$, as shown by two dashed lines, for $R_c W$ changing from 0.6 to $\sim 3 \text{ k}\Omega \mu\text{m}$. This result indicates that R_{sh} plays a dominant role in determining the $R_c W$ in the field-emission region.

We also obtained $R_c W$ for the single-layer (1L)-MoS₂ device (see supplementary Fig. S6 for the thickness profile). In Fig. 3b, the $R_c W$ values were extracted via the TLM with three channels ($L = 0.5, 0.9, 1.4 \mu\text{m}$) as shown in the inset of Fig. 3b. For three $V_{G\text{-th}}$ conditions of $35, 40,$ and 45 V , $R_c W$ decreased with decreasing T in the range $250 \geq T \geq 100 \text{ K}$, representing the field emission. Here, $V_{G\text{-th}} = V_G - V_{th}$ and V_{th} is the threshold voltage. At $V_{G\text{-th}} = 45 \text{ V}$, $R_c W$ reached $\sim 1 \text{ k}\Omega \mu\text{m}$ at T

= 100 K as the minimum value obtained from the 1L-MoS₂ device. This value is similar to that obtained from the 6L-MoS₂ device at a similar T range (see Fig. 2). Interestingly, $R_c W$ increased with decreasing T for $T < 100$ K under all V_{G-th} conditions. In this region, the MoS₂ channel also exhibited an insulating behavior in $G-V_g$ curves for various temperatures of Fig. 3b for $V_G < 60$ V and $T < 100$ K. Thus, it indicates that the increase of R_{sh} with decreasing T in the insulating phase plays a dominant role in determining the contact resistance at $T < 100$ K. This implies that the manipulation of the metal-insulator crossover gate voltage could be crucial to get a better contact property in a single-layer MoS₂ device.

In Fig. 3a we compared the lowest achievable contact resistance as a function of R_{sh} from previous reports with ours. For the In/MoS₂ device, the contact resistance decreased with decreasing R_{sh} and reached ~ 0.6 k Ω μm as the lowest value at $R_{sh} \sim 1$ k Ω and $T = 2.4$ K. At $T = 300$ K, on the other hand, the Au/In/few layer-MoS₂ device showed the lowest value of ~ 0.6 k Ω μm at $R_{sh} \sim 60$ k Ω . Importantly, our In/MoS₂ contact provided 1-2 k Ω μm at $R_{sh} \sim 50$ k Ω as the lowest value for single-layer MoS₂ devices, while the Au/In/few layer-MoS₂ contact showed ~ 3 k Ω μm at $R_{sh} \sim 40$ k Ω .

Accumulation-type contacts at In/MoS₂ interface

We note that both Fig. 1d and Fig. 3b show that the threshold V_G for few-layer and monolayer MoS₂ is located at $V_G \geq 0$ V, which indicates that the Fermi energy E_F of In is located near the conduction-band minimum (CBM) position of MoS₂. Since the electron affinity of MoS₂ (χ_{MoS_2}) ranging from 4 eV (mono-layer MoS₂) to 4.3 eV (multilayer MoS₂) is comparable to the work function of In (Φ_{In}) of ~ 4.1 eV, the vacuum (Schottky-Mott limit) band alignment at the interface

can be expected to be an accumulation type²². To experimentally confirm the electron accumulation at an In-contacted region in MoS₂, we applied the Raman spectroscopy to measure the pristine and In-covered MoS₂ regions. It is known that the A_{1g} phonon peak of MoS₂ exhibit a red shift and its width broadens upon electron doping^{23,24}. Figures 4a and 4b show the optical images of respectively 1L- and bilayer (2L)-MoS₂ (indicated by dashed black lines) prepared on SiO₂ and partially covered with 5 nm-thick In (indicated by dashed white lines). Figures 4c and 4d show the A_{1g} energy maps for the 1L- and 2L-MoS₂, respectively (see also Supplementary Fig. S7 for representative Raman spectra of 1L-MoS₂). The In-covered region shows a relatively lower energy than the non-covered region, i.e., $\Delta\omega \approx -0.3$ and -1 cm^{-1} for the 1L- and 2L-MoS₂, respectively. These red shifts of the A_{1g} energy reflect the electron doping of the MoS₂ under the In metal. Chakraborty et. al.²³ reported that the A_{1g} mode softens with doping at a rate of $\sim 0.2 \text{ cm}^{-1}$ per 10^{12} cm^{-2} for 1L-MoS₂, indicating that the 1L-MoS₂ region covered by In was doped by electrons at a density of $\sim 1.5 \times 10^{12} \text{ cm}^{-2}$. The full-width at half maximum, Γ , in Fig. 4e and 4f also shows consistent results. For instance, the In-covered region shows a relatively broader Γ than the non-covered region for both 1L- and 2L-MoS₂, implying electron doping. The electron doping at the In/MoS₂ contact induces an accumulation-type contact, indicating the feasibility of field emission at the In/MoS₂ contact.

Atomistic origin of low contact resistance at In/MoS₂ interface

To clarify the special characters of indium in forming a vdW contact with MoS₂, we carried out comparative density functional theory (DFT) calculations for the vertical In/MoS₂ and Au/MoS₂ interface models shown in Fig. 5a. Shown together are the real-space charge density differences at the metal/MoS₂ interfaces calculated from the fully geometry-optimized models according to

$$\Delta\rho = \rho_{metal/MoS_2} - (\rho_{MoS_2} + \rho_{metal}). \quad (2)$$

We observe that, compared with the Au case, In induces much less charge transfer and concomitantly less structural distortions on MoS₂ (also see Supplementary Fig. S7). In addition, the direction of charge transfer in the In/MoS₂ contact was different from that in the Au/MoS₂ counterpart, and quantitatively the amounts of charge transfer from metal to MoS₂ were $+4.1 \times 10^{12}$ electrons/cm² and -2.5×10^{13} electrons/cm² for the In and Au cases, respectively. This indicates that In exhibits a relatively weak interactions with MoS₂ compared with Au. Moreover, the doping level calculated from the In/MoS₂ interface model is in good quantitative agreement with that estimated from Raman measurements, confirming the accuracy of our computational scheme (see Supplementary Fig. S8 for more details including additional consistency checks).

We next analyze the electronic structures of the In/MoS₂ interface in two steps. First, for the vertical In/MoS₂ model adopted above that represents the deep contact region (see Fig. 5b top panel), we calculated the projected density of states (DOS) and monitored how the In-5p_z states evolve into the top S-3p, Mo-4d, and bottom S-3p states (Fig. 5b bottom panels). We note that a noticeable amount of metal-induced gap states (MIGS) appear in the In-contacting top S layer as well as the Mo layer (indicated by blue arrows). Particularly, around the MoS₂ conduction band minimum (CBM) region located around the In Fermi level E_F (indicated by a red arrow), we observe ample Mo-4d states, which identifies the origin of the experimentally observed Ohmic transport behavior.

Because the vertical interface model is not sufficient to capture the development of the electrode-region MoS₂ electronic structure into that of the channel-region MoS₂, we next adopted a junction model shown in Fig. 5c top panel (see also Supplementary Fig. S9a) and carried out DFT-based matrix Green's function (MGF) calculations^{25,26}. From the spatially-resolved DOS

shown in Fig. 5c bottom panel, we immediately note that the above-discussed MIGS formed within the In-covered region (A, red upward triangle) propagates about ~ 1 nm into the channel region (B, blue upward triangle) before the intrinsic semiconducting channel region is recovered (C, green upward triangle). Importantly, taking the intrinsic MoS₂ channel region C as the reference, we can clarify the nature of the MoS₂ states around E_F within the In-covered region A (Fig. 5b) as follows (see also Supplementary Information Fig. S9b): Forming an ideal FLP-free In/MoS₂ vdW contact, the respective vacuum-level electronic structures of In and MoS₂ (Fig. 5d; $\Phi_{\text{In}} \approx 4.1$ eV and $\chi_{1\text{L MoS}_2} \approx 4.2$ eV) hint the possibility of achieving an Ohmic behavior. However, the In-to-MoS₂ electron transfer should cause a band upshift, which then places the CBM of the intrinsic C-region MoS₂ at ~ 0.24 eV above E_F . The pure electrostatic argument can then predict the development of MoS₂ band from In to MoS₂ region A to MoS₂ region B in terms of the band bending picture such as given in Fig. 5e or Fig. 5f^{6,7}. While the presence of MoS₂ states around E_F in Fig. 5c might appear supporting this picture, a close inspection in fact presents another viewpoint as schematically summarized in Fig. 5g. Here, as is evident from the fact that the valence band maximum edge in region A does not bend upward into regions B and C in Fig. 5c, the upshift of MoS₂ band to the level expected in the intrinsic MoS₂ region C (+ 0.24 eV) should have abruptly occurred across the In-MoS₂ vdW gap. Then, the A-region MoS₂ states around E_F in Fig. 5c, which were identified as the source of the Ohmic In/MoS₂ vdW contact, can be interpreted as the below-CBM MIGS rather than the bent-down CBM states, as depicted by thick red lines in Fig. 5g.

Conclusion

In summary, we realized for the first time an Ohmic vdW contact between the 3D elemental metal In and 2D semiconductor MoS₂ by applying the low thermal-energy In deposition process

while keeping the substrate holder at ~ 100 K. For the single- and few-layer MoS₂ devices, the contact resistance decreased with decreasing temperatures for $100 \leq T \leq 300$ K, indicating the field-emission mechanism for the Ohmic contact transport. The contact resistance was sensitive to the change of sheet resistance of MoS₂, rather than that of the specific contact resistivity within the field-emission region. For the single-layer MoS₂ case, we achieved the contact resistance of $\sim 1 \text{ k}\Omega \mu\text{m}$ at $T = 100$ K, which is the lowest value reported by metal evaporations on MoS₂. Our experimental findings were corroborated by *ab initio* DFT and DFT-MGF calculations. Comparison with theory showed that the In metal weakly interacts with MoS₂, or an ideal In/MoS₂ contact is a relatively FLP-free interface with an Ohmic *n*-type band alignment. Importantly, we showed that the band upshift across the In/MoS₂ vdW gap is abrupt and rigid, while the below-CBM states that contribute to the Ohmic transport can be attributed to MIGS.

Methods

TEM imaging A cross-sectional TEM sample was prepared by the dual-beam focused ion beam (Helios, FEI). HR-FE-TEM (JEM-2100F, JEOL) was used for the TEM imaging at 200 kV.

Raman spectrum The Raman measurements were performed in a backscattering geometry at room temperature. An incident laser light with a wavelength of 514.5 nm was focused on the sample surface through an optical microscope objective lens (100 \times /0.9 NA). An excitation laser power was maintained less than 0.4 mW to avoid any laser-induced heating effects. Scattered light from the sample was dispersed through a monochromator with a 1200 grooves/mm grating and was collected using a thermoelectrically cooled charge-coupled device detector. For mapping measurements, Raman spectra were taken at the step of 0.5 μm over the area of $15 \times 15 \mu\text{m}^2$.

Electrical measurements To apply an electric field to the MoS₂ channel, the highly *p*-doped Si substrate was biased by a back-gate voltage (V_G). All measurements were performed in a cryostat (PPMS, Quantum Design, Inc.) with a base T of 2.4 K. The I - V_{SD} curves were measured by a DC bias voltage source (Yokogawa 7651) combined with a current pre-amplifier (DL 1211). The two-probe and four-probe conductance measurements for 1L-MoS₂ device were performed by a dc measurement setup. The two-probe and four-probe conductance measurements for 6L-MoS₂ device were performed by using a standard lock-in amplifier (SR830) with current preamplifier, where excitation voltage and output frequency were 30 mV and 77.77 Hz, respectively.

DFT and DFT-MGF calculations. We adopted the VASP software²⁷ to carry out DFT geometry optimizations for the metal/MoS₂ slab models within the Grimme DFT-D3 scheme²⁸ until the Hellmann-Feynman forces were below $0.02 \text{ eV} \cdot \text{\AA}^{-1}$. We then calculated their electronic structure using the SIESTA software²⁹ within the vdW-DF2 functional.³⁰ To avoid artificial interactions with neighbour unit cell images within the periodic boundary condition, we inserted a vacuum space of more than 15 \AA along the slab-normal direction. For the quantum transport calculations, we constructed the junction models starting from the In/Mo₂ models described above (Fig. 5c; see also Supplementary Fig. S9) and carried out DFT-MGF calculations using the TransSIESTA code.³¹ We confirmed that the computational results are not modified by adopting a different exchange-correlation functional (Supplementary Table 1). More details of DFT and DFT-MGF calculations can be found in Supplementary Fig. S10.

Acknowledgments

We acknowledge Prof. E. Hwang and Dr. J.-S. Park for fruitful discussion. This work was supported by the Korea Research Institute of Standards and Science (KRISS-GP2018-003), part of

the Basic Science Research Program through the National Research Foundation of Korea (NRF) (Grant Nos. 2018R1A2A1A05078440, SRC2016R1A5A1008184, 2016R1A2B4008525 and 2019R1A2C1003366). This work was also partly supported by the Korea-Hungary Joint Laboratory Program for Nanosciences through the National Research Council of Science and Technology. Growth of hexagonal boron nitride crystals was supported by the Elemental Strategy Initiative conducted by the MEXT, Japan and JSPS KAKENHI Grant Numbers JP15K21722. Y.-H.K. and T.H.K were supported by the NRF grants (Basic Research Program 2017R1A2B3009872, Nano-Material Technology Program 2016M3A7B4024133, Global Frontier Program 2013M3A6B1078881, and Basic Research Lab Program 2017R1A4A1015400). Computational resources were provided by the KISTI Supercomputing Center (KSC-2018-C2-0032).

Author contributions

M.-H.B. and J.-J.K conceived the research project and Y.-H.K provided the theoretical interpretation. K.W. and T.T grew the bulk hBN. D.-H.C and B.-K.K fabricated the devices. D.-H.C performed the TEM analysis. B.-K.K performed the electrical measurements and analysed the data with M.-H.B. H.K. and H.R. performed the Raman spectroscopy. T.-H.K performed DFT and DFT-MGF calculations. All authors wrote the manuscript.

References

1. Liu, Y. *et al.* Approaching the Schottky-Mott limit in van der Waals metal-semiconductor junctions. *Nature* **557**, 696–700 (2018).

2. Wang, Y. *et al.* Van der Waals contacts between three-dimensional metals and two-dimensional semiconductors. *Nature* **568**, 70 (2019).
3. Manzeli, S., Ovchinnikov, D., Pasquier, D., Yazyev, O. V. & Kis, A. 2D transition metal dichalcogenides. *Nat. Rev. Mater.* **2**, 17033 (2017).
4. Li, C., Zhou, P. & Zhang, D. W. Devices and applications of van der Waals heterostructures. *J. Semicond.* **38**, 31005 (2017).
5. Xia, F., Wang, H., Xiao, D., Dubey, M. & Ramasubramaniam, A. Two-dimensional material nanophotonics. *Nat. Photonics* **8**, 899 (2014).
6. Allain, A., Kang, J., Banerjee, K. & Kis, A. Electrical contacts to two-dimensional semiconductors. *Nat. Mater.* **14**, 1195–1205 (2015).
7. Schulman, D. S., Arnold, A. J. & Das, S. Contact engineering for 2D materials and devices. *Chem. Soc. Rev.* **47**, 3037–3058 (2018).
8. Das, S., Chen, H.-Y., Penumatcha, A. V. & Appenzeller, J. High performance multilayer MoS₂ transistors with scandium contacts. *Nano Lett.* **13**, 100–105 (2012).
9. Kim, C. *et al.* Fermi level pinning at electrical metal contacts of monolayer molybdenum dichalcogenides. *ACS Nano* **11**, 1588–1596 (2017).
10. Yang, L. *et al.* Chloride molecular doping technique on 2D Materials: WS₂ and MoS₂. *Nano Lett.* **14**, 6275 (2014).
11. Wang, J. *et al.* High mobility MoS₂ transistor with Low Schottky barrier contact by using atomic thick h-BN as a tunneling layer. *Adv. Mater.* **28**, 8302–8308 (2016).
12. Cui, X. *et al.* Low-temperature Ohmic contact to monolayer MoS₂ by van der Waals bonded Co/h-BN electrodes. *Nano Lett.* **17**, 4781 (2017).

13. Cui, X. *et al.* Multi-terminal transport measurements of MoS₂ using a van der Waals heterostructure device platform. *Nat. Nanotechnol.* **10**, 534–540 (2015).
14. Leong, W. S., Luo, X., Khoo, K. H., Quek, S. Y. & Thong, J. T. L. Low resistance metal contacts to MoS₂ devices with nickel-etched-graphene electrodes. *ACS Nano* **9**, 869–877 (2015).
15. Kappera, R. *et al.* Phase-engineered low-resistance contacts for ultrathin MoS₂ transistors. *Nat. Mater.* **13**, 1128–1134 (2014).
16. Dean, C. R. *et al.* Boron nitride substrates for high-quality graphene electronics. *Nat. Nanotechnol.* **5**, 722–726 (2010).
17. Choi, D.-H. *et al.* Van-der-Waals-gap tunneling spectroscopy for single-wall carbon nanotubes. *Carbon N. Y.* **113**, 237–242 (2017).
18. Fivaz, R. & Mooser, E. Mobility of charge carriers in semiconducting layer structures. *Phys. Rev.* **163**, 743–755 (1967).
19. Kim, S. *et al.* High-mobility and low-power thin-film transistors based on multilayer MoS₂ crystals. *Nat. Commun.* **3**, 1011–1017 (2012).
20. English, C. D., Shine, G., Dorgan, V. E., Saraswat, K. C. & Pop, E. Improved contacts to MoS₂ transistors by ultra-high vacuum metal deposition. *Nano Lett.* **16**, 3824–3830 (2016).
21. Xia, F., Perebeinos, V., Lin, Y. M., Wu, Y. & Avouris, P. The origins and limits of metal-graphene junction resistance. *Nat. Nanotechnol.* **6**, 179–184 (2011).
22. Tung, R. T. The physics and chemistry of the Schottky barrier height. *Appl. Phys. Rev.* **1**, 11304 (2014).

23. Chakraborty, B. *et al.* Symmetry-dependent phonon renormalization in monolayer MoS₂ transistor. *Phys. Rev. B* **85**, 161403 (2012).
24. Somvanshi, D. *et al.* Nature of carrier injection in metal/2D-semiconductor interface and its implications for the limits of contact resistance. *Phys. Rev. B* **96**, 205423 (2017).
25. Kim, Y. H. & Kim, H. S. Anomalous length scaling of carbon nanotube-metal contact resistance: An ab initio study. *Appl. Phys. Lett.* **100**, 213113 (2012).
26. Kim, H. S., Kim, H. S., Lee, G. I., Kang, J. K. & Kim, Y. H. Intrinsically low-resistance carbon nanotube-metal contacts mediated by topological defects. *MRS Commun.* **2**, 91–96 (2012).
27. Kresse, G. & Joubert, D. From ultrasoft pseudopotentials to the projector augmented-wave method. *Phys. Rev. B* **59**, 1758-1775 (1999).
28. Grimme, S., Ehrlich, S. & Goerigk, L. Effect of the damping function in dispersion corrected density functional theory. *J. Comput. Chem.* **32**, 1456 (2011).
29. Soler J.M. *et al.* The SIESTA method for ab initio order-N materials simulation. *J. Phys. - Condens. Matter* **14**, 2745–2779. (2002).
30. Lee, K., Murray, E. D., Kong, L., Lundqvist, B. I., and Langreth, D. C. Higher-accuracy van der Waals density functional. *Phys. Rev. B* **82**, 081101 (2010).
31. Brandbyge, M., Mozos, J. L., Ordejón, P., Taylor, J. & Stokbro, K. Density-functional method for nonequilibrium electron transport. *Phys. Rev. B* **65**, 165401 (2002).

Figure captions

Figure 1| Characterization and electrical properties of In/MoS₂ devices. **a**, In (Au) evaporation in a vacuum chamber with a liquid-nitrogen cooled sample holder. **b**, Top and bottom: cross-sectional TEM image of the In/MoS₂ and Au/MoS₂ interfaces, respectively. Scale bar: 5 nm. **c**, Optical image of a 6L-MoS₂/hBN device with multiple In contacts. Scale bar: 5 μm. **d**, Conductance (G) as a function of the back-gate voltage (V_G) at various temperatures.

Figure 2| Contact and sheet resistance of an In/6L-MoS₂ device. **a**, R_cW as a function of carrier density (n_e) of In/6L-MoS₂ device at various temperatures (scattered solid squares) with previous works (solid curves: graphene(Gr)/4L-MoS₂, opened diamonds: Au/4L-MoS₂, opened pentagons: Au/In/few L-MoS₂). **b**, R_cW and R_{sh} as a function of T at $n_e = 3.4 \times 10^{12} \text{ cm}^{-2}$.

Figure 3| Contact resistance vs. sheet resistance and R_cW of 1L-MoS₂. **a**, Minimum R_cW as a function of sheet resistance (R_{sh}) of In/6L-MoS₂ device at various temperatures (scattered solid squares) with previous works (opened triangles: graphene(Gr)/4L-MoS₂, opened diamonds: Au/4L-MoS₂, opened pentagons: Au/In/few (1) L-MoS₂). The upper and lower dotted lines were obtained with $\rho_c = 5 \times 10^{-6} \Omega \text{ cm}^2$ and $5 \times 10^{-7} \Omega \text{ cm}^2$, respectively. **b**, Four-probe $G-V_G$ curves at various temperatures obtained from the $L = 1 \mu\text{m}$ channel, indicated by a dashed box in the inset of **b**. The inset of **b**: AFM image of a 1L-MoS₂ device with four In electrodes. The region outlined by a solid white line indicates the MoS₂ flake. Scale bar: 5 μm. **c**, R_cW-T curves corresponding to various V_{G-th} conditions.

Figure 4| Electron accumulation-type contact and Raman mapping of In/1L- and In/2L-MoS₂. **a,b**, Optical images of 1L- and 2L-MoS₂ (dashed black-boxed region) on SiO₂ substrates, respectively. White boxed regions: 5 nm-thick In-deposited regions. Scale bar: 5 μm . **c,d**, A_{1g} energy (ω) maps for 1L- and 2L-MoS₂, respectively. **e,f**, Full-width at half-maximum (I) maps of A_{1g} for 1L- and 2L-MoS₂, respectively.

Figure 5| DFT and DFT-based matrix Green's function calculations at In(Au)/MoS₂ interface. **a**, DFT-optimized geometries and interfacial charge transfers obtained from the In/MoS₂ (top) and Au/MoS₂ (bottom) interface models. Red and blue colors represent the charge accumulation and depletion regions, respectively. The isosurface level is $0.0007 \text{ e}/\text{\AA}^3$. **b**, For the In/MoS₂ interface model (top panel; the red dashed box indicates the supercell atomic structure for DFT calculations), we show the projected DOS (bottom panel) of the top S $3p$ states (bottom left panel), Mo $4d$ states (bottom central panel), and bottom S $3p$ states (bottom right panel). Shown together is the bottommost In $5p_z$ states (filled curves). The arrows indicate the prominent MIGS. **c**, Half of the In/MoS₂/In junction model adopted for DFT-MGF calculations (top panel) and the calculated local DOS (bottom panel). The red (A), blue (B), and green (C) upper triangles indicate the In-contact, interface, and intrinsic channel MoS₂ regions, respectively. CBM and VBM indicate the conduction band minimum and valance band maximum, respectively. **d**, Schematics of the In and MoS₂ band levels before contact. **e** and **f**, Schematics of the previously proposed band alignments for vdW contacts based on the band bending. **g**, Schematic band alignment derived from our DFT-MGF calculations (Fig. 5c). Here, the red lines represent MIGS.

Figures

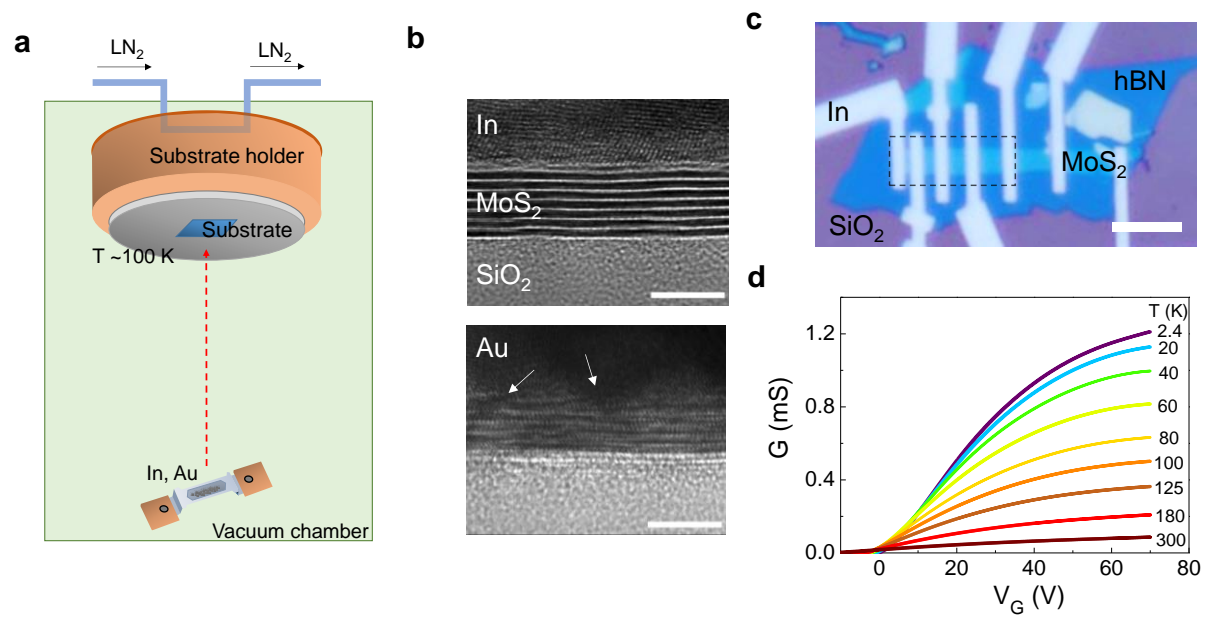


Figure 1

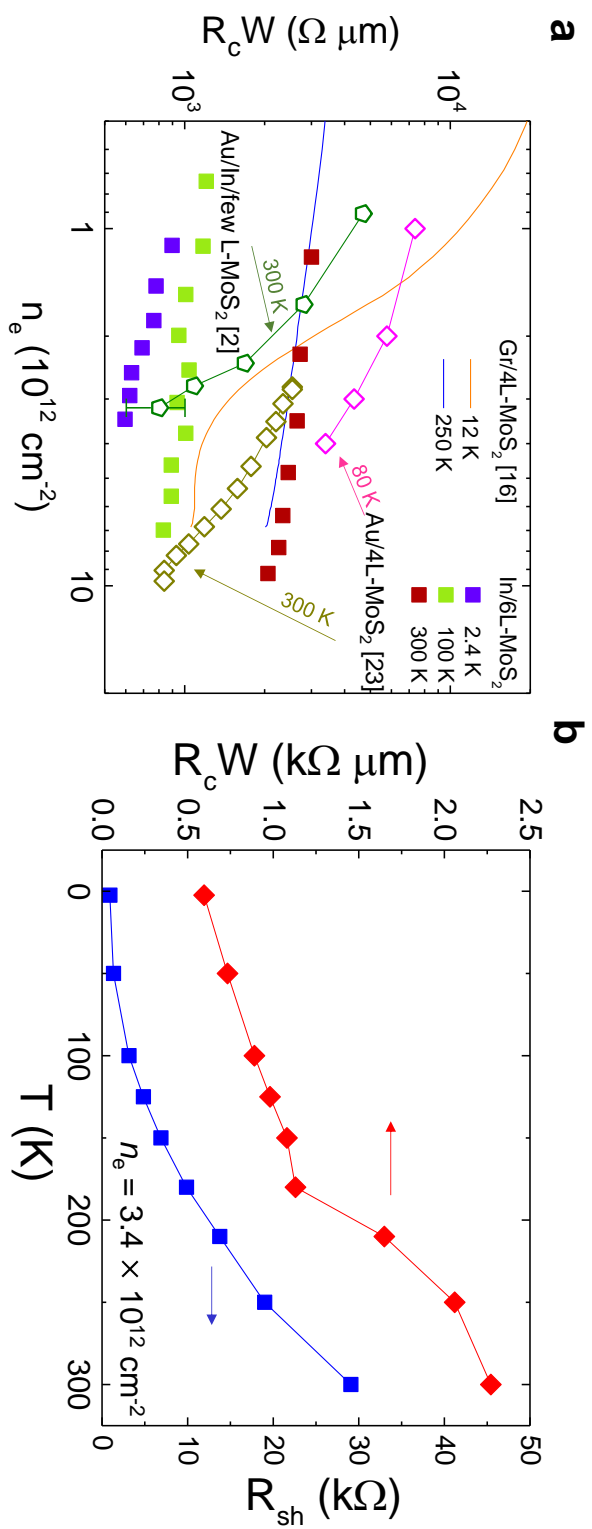


Figure 2

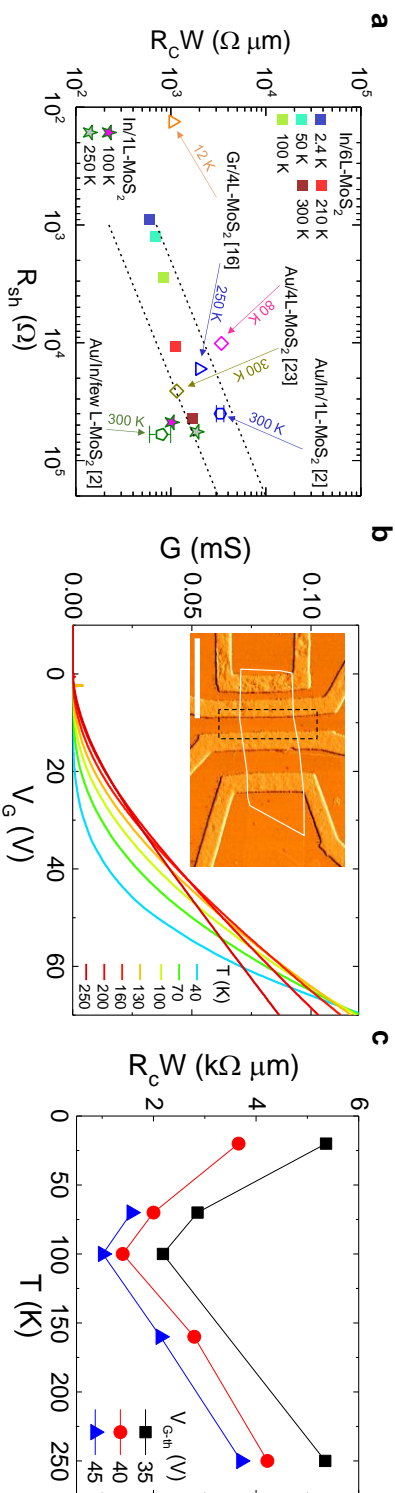


Figure 3

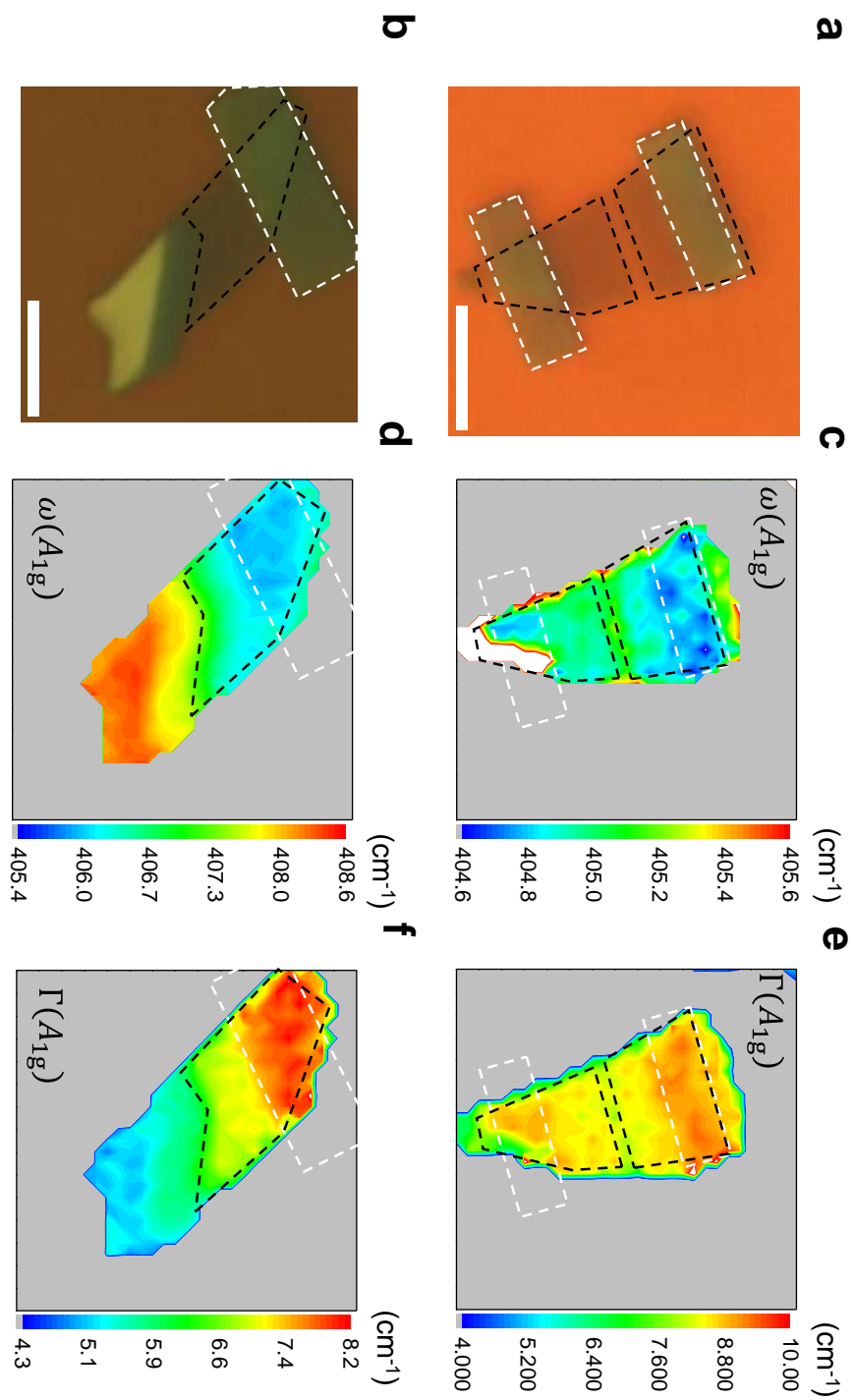


Figure 4

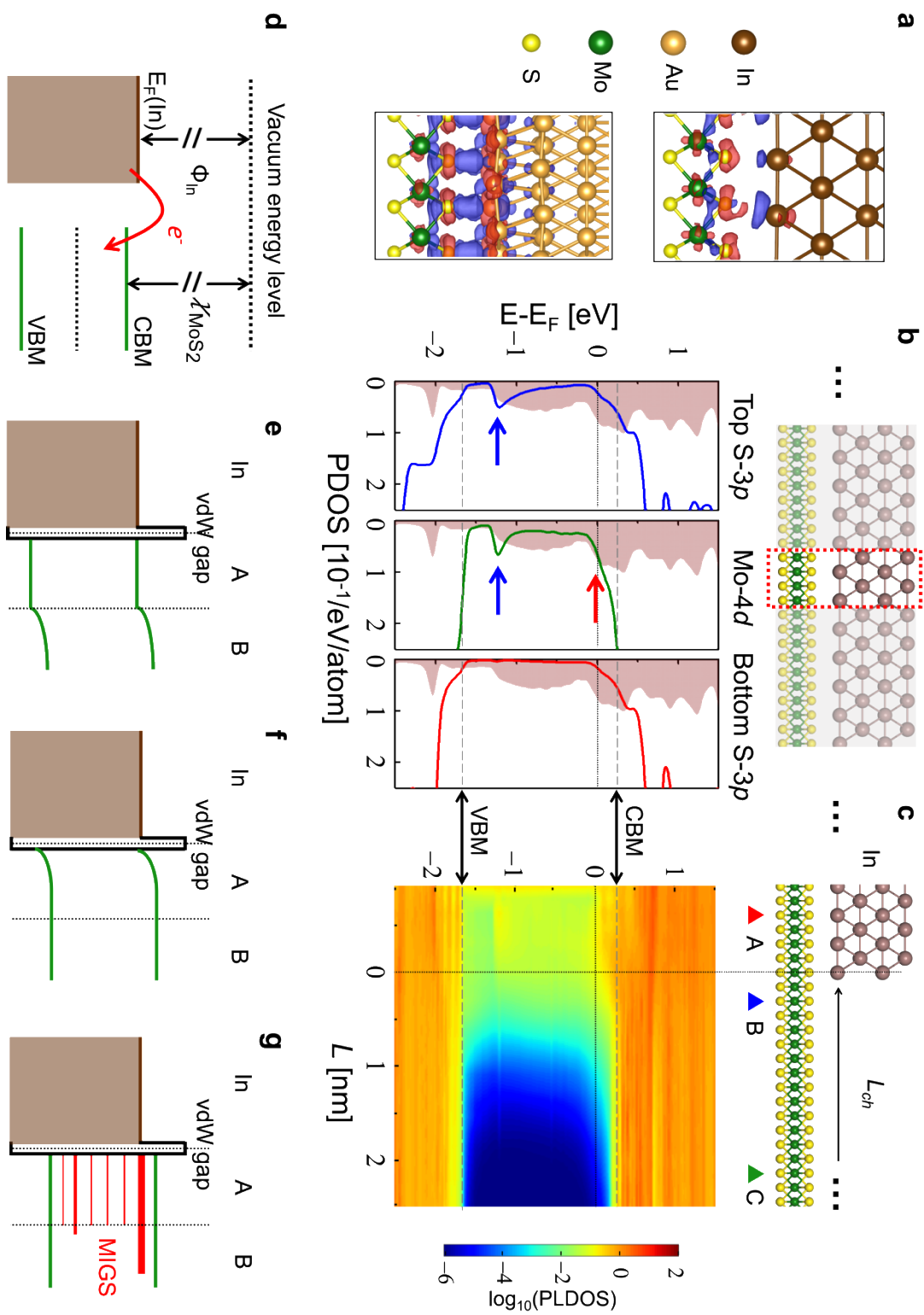


Figure 5

Supplementary Information for

Genuine Ohmic van der Waals contact between indium and MoS₂

Bum-Kyu Kim^{1†}, Dong-Hwan Choi^{1,2†}, Tae-Hyung Kim^{3†}, Hanul Kim², Kenji Watanabe⁴, Takashi Taniguchi⁴, Heesuk Rho², Yong-Hoon Kim^{3*}, Ju-Jin Kim^{2*}, and Myung-Ho Bae^{1,5*}

¹Korea Research Institute of Standards and Science, Daejeon 34113, Republic of Korea

²Department of Physics, Research Institute of Physics and Chemistry, Chonbuk National University, Jeonju 54896, Republic of Korea

³School of Electrical Engineering, Korea Advanced Institute of Science and Technology, 291 Daehak-ro, Yuseong-gu, Daejeon 34141, Republic of Korea

⁴National Institute for Materials Science, 1-1 Namiki, Tsukuba 305-0044, Japan

⁵Department of Nano Science, University of Science and Technology, Daejeon, 34113, Republic of Korea

†These authors contributed equally to this work.

*e-mail: y.h.kim@kaist.ac.kr; jujinkim@chonbuk.ac.kr; mhbae@kriss.re.kr

Section 1. Six-layer (6L) MoS₂ device

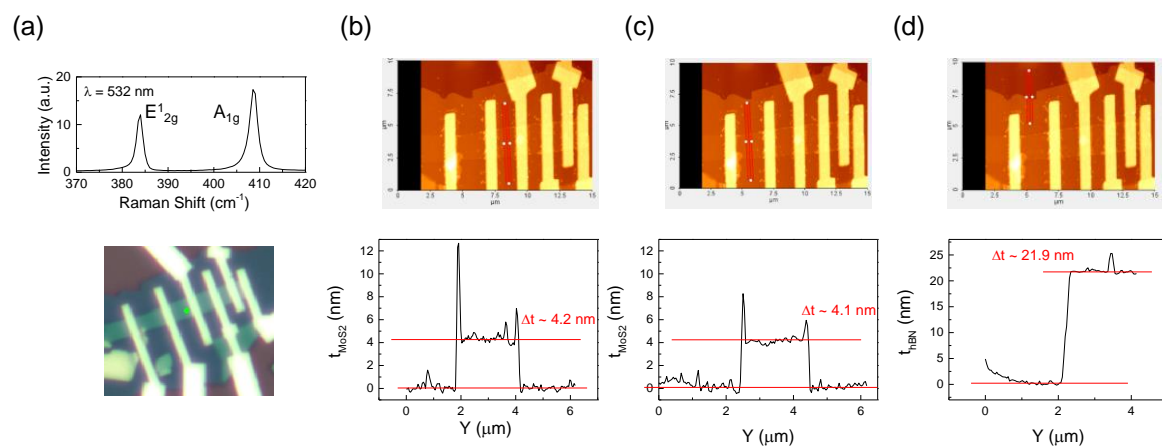


Figure S1. (a) Raman spectrum of 6L-MoS₂ device (upper panel), which was taken at the green spot in a photo-image of the lower panel. (b)-(d) upper panels: AFM images of the device. Lower panels: thickness profile along the red boxes in the corresponding upper panels ((b),(c): MoS₂, (d): hBN).

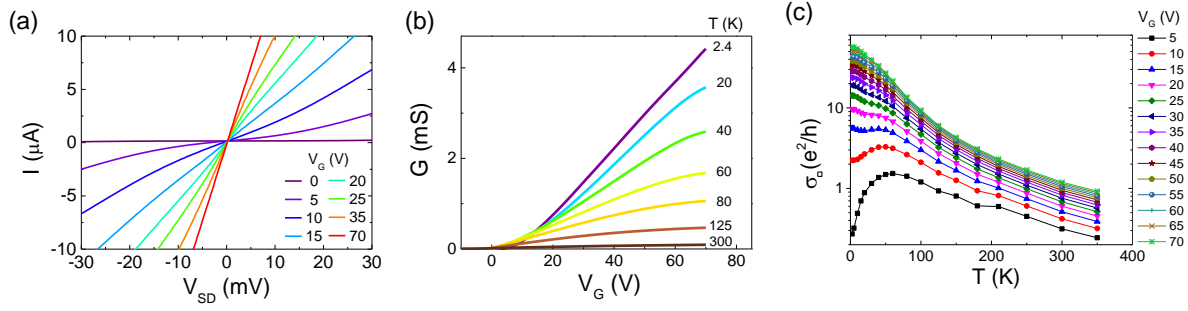


Figure S2. (a) Current (I) as a function of the source–drain voltage (V_{SD}) for various V_{G} at $T = 2.4$ K. (b) 4-probe G - V_{G} curves of 6L-MoS₂ device for various temperatures. (c) Normalized conductance as a function T for various V_{G} . For $V_{\text{G}} > 15$ V corresponding to the crossover temperature between the metal and insulator characters, the down-turn curvature for $T < 70$ K was disappeared.

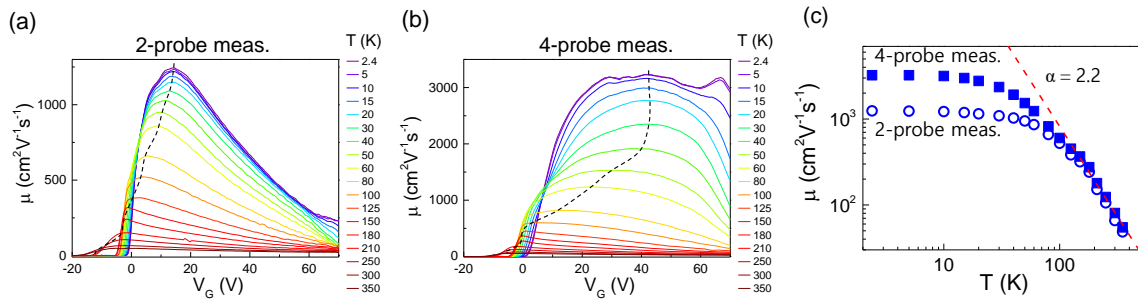


Figure S3. Mobility (μ) as a function of V_G at various temperatures for (a) two-probe and (b) four-probe measurements. The dashed lines traces the local maximum mobility for varying T . The mobility was obtained by a relation of $\mu = \frac{L}{W} \frac{1}{C_G} \frac{dG}{dV_G}$, where L and W are channel length and width, respectively, and C_G ($= (C_{\text{SiO}_2}^{-1} + C_{\text{hBN}}^{-1})^{-1}$) is the back-gate capacitance. (c) μ as a function of temperature (T) on a log scale, as obtained from 2-probe (open circles) and 4-probe (closed squares) measurements. The dashed line is a fitting line with a relation of $\mu(T) \propto T^{-\alpha}$ ($\alpha = 2.2$).

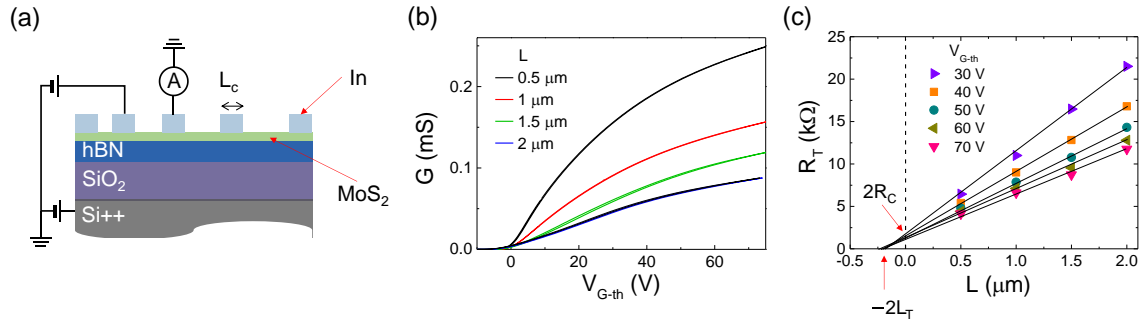
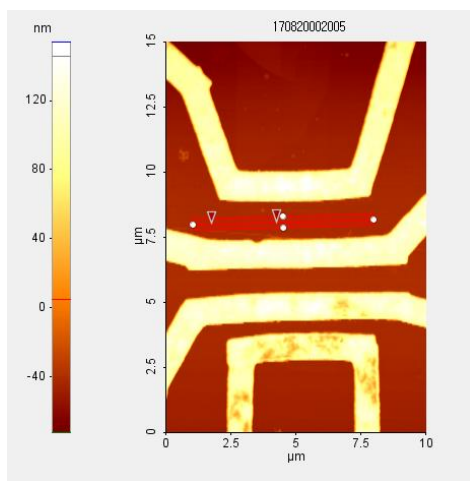


Figure S4. (a) Schematic of 6L-MoS₂ device for the transfer length method (TLM). Here, $L_c (= 1 \mu\text{m})$ is the length of contact electrode. The measurement scheme shows the two-probe measurement for the $L_2 = 1 \mu\text{m}$ channel. (b) Conductance as a function of $V_{G\text{-th}}$ for the four channels at $T = 210 \text{ K}$. (c) Total resistance (R_T) as a function channel length L for representative $V_{G\text{-th}}$ values at $T = 210 \text{ K}$. R_c and L_T are the contact resistance and transfer length, respectively. These are indicated by arrows at $V_{G\text{-th}} = 30 \text{ V}$, as an example. L_T was estimated as $\sim 0.1 \mu\text{m}$.

Section 2. Single-layer (1L) MoS₂ device

(a)



(b)

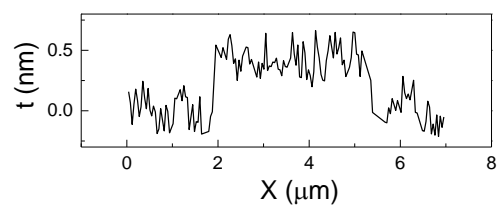


Figure S5. (a) AFM image of 1L-MoS₂ device. (b) Thickness profile along the red line in (a).

Section 3. 1L-MoS₂ to study the doping effect by In contacts

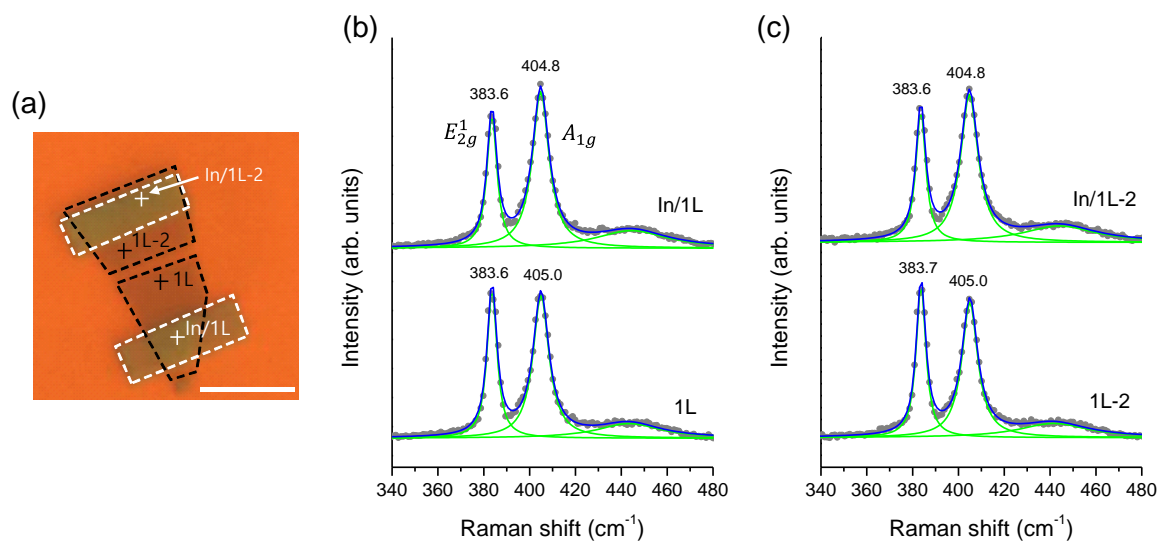


Figure S6. (a) Optical photo-image of a 1L-MoS₂ (outlines: dashed black lines) on SiO₂ with indium contacts (dashed white lines). (b) and (c) Scattered points: Raman spectra obtained at white (In/1L) and black (1L) cross marks in (a). Green and blue curves are Lorentzian-fit results to estimate the energy and width of phonon modes.

Section 4. First-principles density functional theory (DFT) and matrix Green's function (MGF) calculations

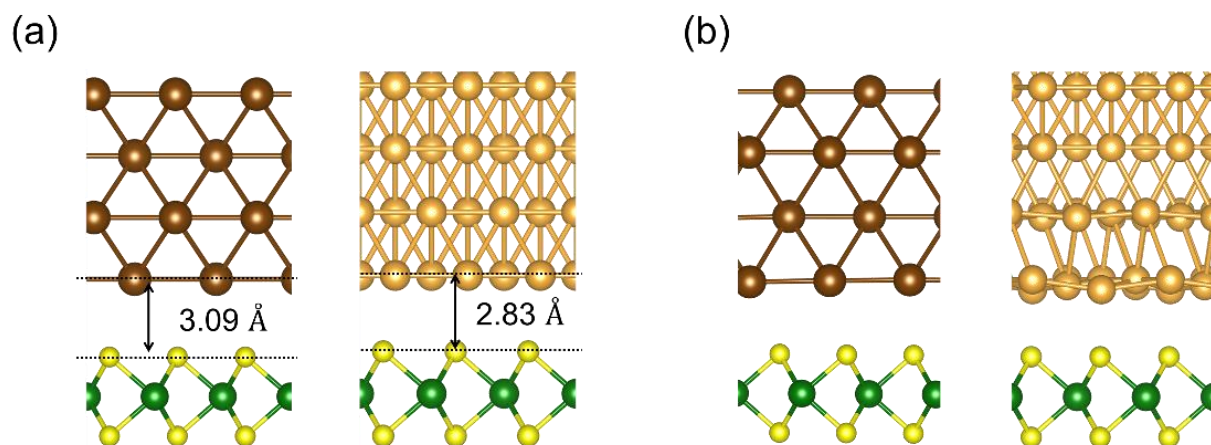


Figure S7. (a) Vertical interface model of In/MoS₂ (left panel) and Au/MoS₂ (right panel) before geometry optimization. Here, the MoS₂-metal distance was determined with Grimme DFT-D3 method. (b) Optimized structures for In/MoS₂ (left panel) and Au/MoS₂ (right panel), respectively.

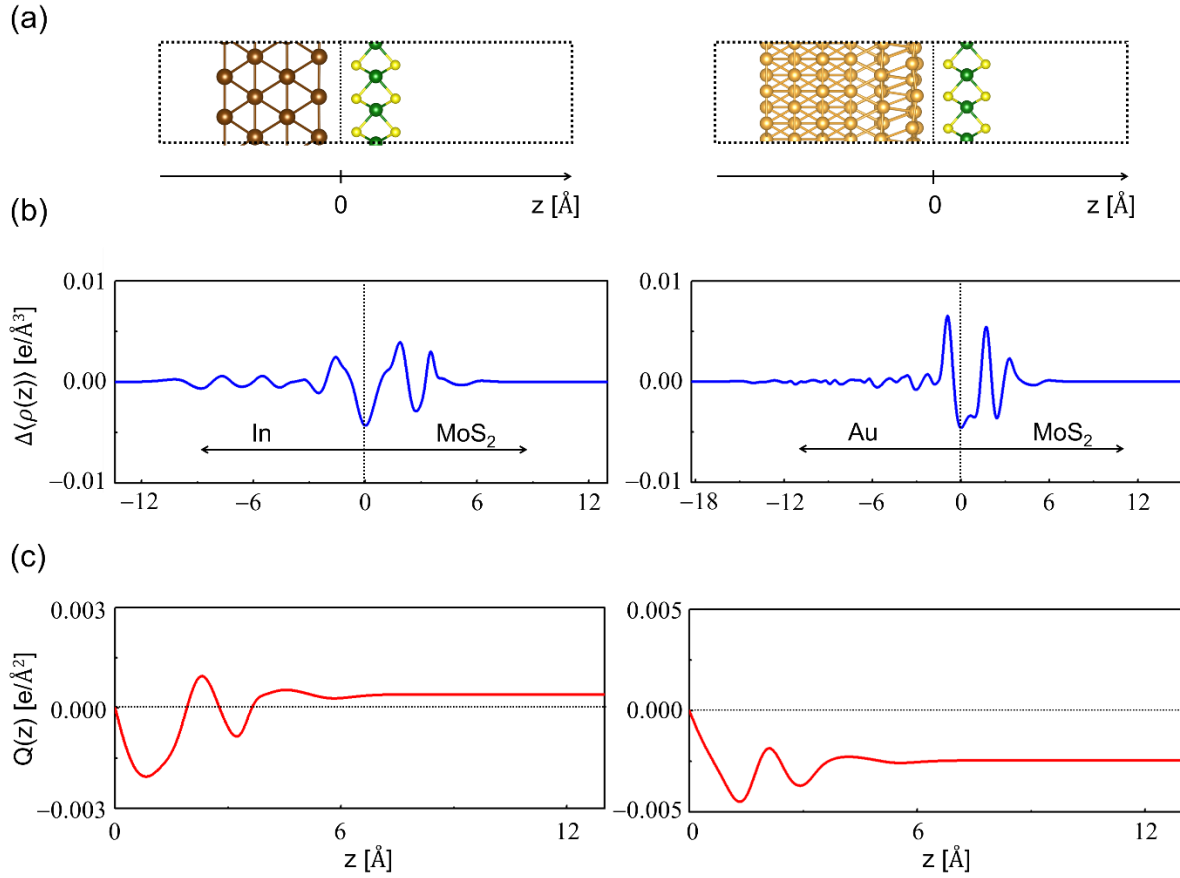


Figure S8. (a) Vertical In(Au)/MoS₂ model (from left to right). (b) Plane averaged charge density difference ($\Delta\langle\rho\rangle = \langle\rho_{Total}\rangle - \langle\rho_{MoS_2}\rangle - \langle\rho_{Metal}\rangle$) for the vertical In(Au)/MoS₂ model (from left to right). We chose a reference position ($z=0$) at the minimum $\Delta\langle\rho\rangle$ position at the metal-S interface. (c) Net charge transfer $Q(z)$ from In(Au) to the MoS₂, which are calculated according to $Q(z) = \int_0^{z_{vacuum}} \Delta\langle\rho(z')\rangle dz'$. The positive (negative) $Q(z)$ indicates an electron transfer from metal to MoS₂ (from MoS₂ to metal).

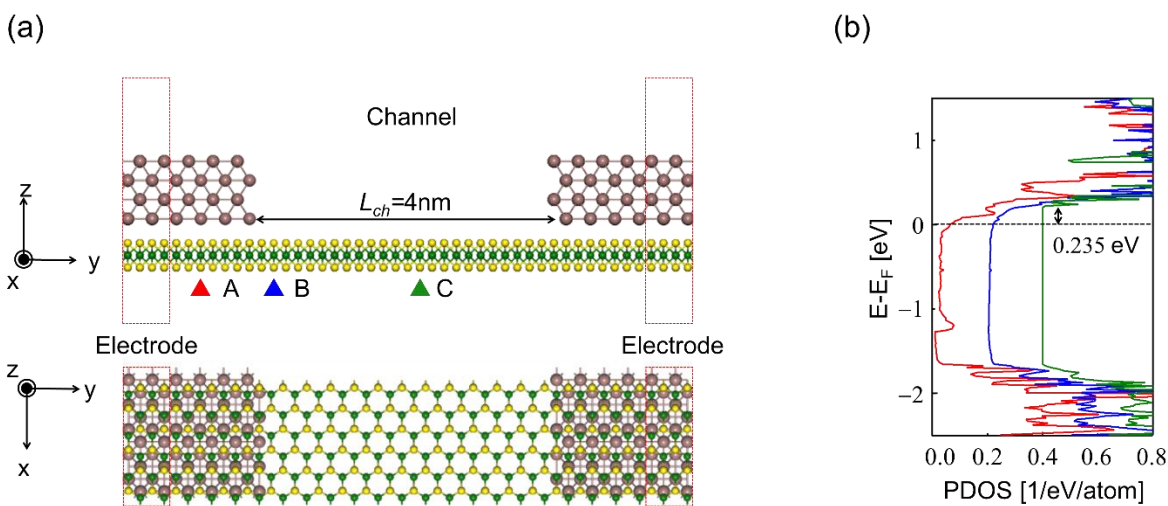


Figure S9. (a) Models for the MGF calculations for the In/MoS₂/In junction. Here, red-dashed rectangular boxes indicate the semi-infinitely repeated left and right electrode parts within quantum transport calculations. The A, B, and C upper triangles indicate the electrode contact-region, transition-region, and intrinsic channel-region MoS₂ positions, respectively. (b) MGF-calculated Mo-4*d* projected local density of states (PLDOS). The red, blue, and green lines correspond to the Mo-4*d* PLDOS at A, B, and C positions, respectively. The zero of energy is shifted by 0.2 eV and 0.4 eV for the PLDOS at B and C positions, respectively.

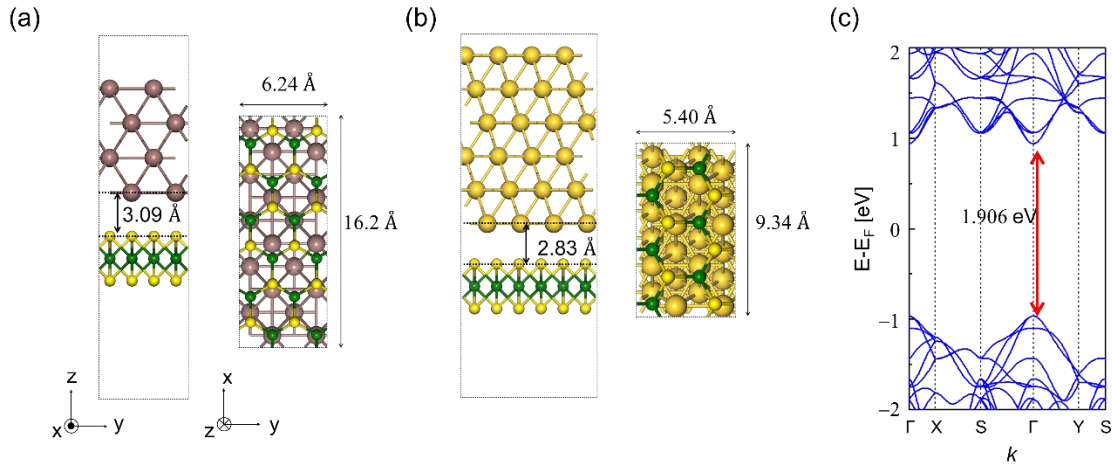


Figure S10. DFT and DFT-MGF calculation details. DFT calculation models: (a) In/MoS₂ and (b) Au/MoS₂. (c) Band structure for pristine single layer MoS₂ in the Au/MoS₂ cell box. Each structure of Au, In, MoS₂ was obtained from local density approximation (LDA)¹ calculation, since each structure is homogenous. Then, we made vertical interface models and the junction model for quantum transport calculation. Here, we adopted the lattice parameters for the heterostructure models as the lattice parameters of MoS₂. The lattice mismatch for In-MoS₂ and Au-MoS₂ is 0.31% and 6.58%, respectively. Then, a MoS₂-metal distance was determined with Grimme DFT-D3 scheme² to capture van der Waals (vdW) interaction. After modelling, we adopted the vdW-DF2 functional³ to capture non-local vdW interaction in the electronic structures. All electronic structures were obtained from vdW-DF2. Next, we confirmed that the pristine single layer MoS₂ has a direct band gap (~1.9 eV) with vdW-DF2, which is well matched previous study⁴. During DFT and MGF calculations, the atomic cores were replaced by norm-conserving nonlocal pseudopotentials of the Troullier-Martins type. Then, we adopted the double ζ -plus-polarization-level numerical atomic orbital basis sets with 30 meV energy cut-off for MoS₂. Meanwhile, we chose the optimized basis cut-off values for each metal in order to correctly describe metal work function. Then, we chose a k -points mesh for In/MoS₂, Au/MoS₂, and In/MoS₂/In as

Functional	Metal	WF [eV]	χ_{MoS_2} [eV]	E_g [eV]
vdW-DF2	In	4.121	4.189	1.906
	Au	5.137	4.189	1.906
LDA	In	4.112	4.196	1.941
	Au	5.130	40196	1.941
	Metal	Q [$e/\text{\AA}^2$]	$\Delta V_{H \text{MoS}_2-M}$ [eV]	BH _C [eV]
vdW-DF2	In	3.61×10^{-4}	0.422	0.235
	Au	-1.97×10^{-3}	-0.411	0.537
LDA	In	7.19×10^{-4}	0.525	0.334
	Au	-1.27×10^{-3}	-0.219	0.630

Table S1. Comparison with vdw-DF2 and LDA results for the vertical In(Au)/MoS₂ interface models. Here, we used an ideal van der Waals contact models as shown in Fig. S9a and 10a, b. We compare the metal work functions (WF), electron affinity for MoS₂ (χ_{MoS_2}), band gap for pristine single layer MoS₂ (E_g), net charge transfer from metal to MoS₂ ($Q(z)$), electrostatic potential difference between MoS₂ and metal ($\Delta V_{H|\text{MoS}_2-M}$), and barrier height for region C (BH_C) in the junction model (Fig. S9). Specifically, we calculated the amount of net charge transfer, $Q(z)$ with same criterion as mentioned in Fig. S8. Next, the plane averaged electrostatic potential difference between MoS₂ and metal was calculated as following equation, $\Delta V_{H|\text{MoS}_2-M} = \Delta V_{H|\text{MoS}_2} - \Delta V_{H|\text{Metal}}$, where the plane averaged electrostatic potential was calculated as $\Delta V_H = V_{H|\text{Total}} - (V_{H|\text{Metal}} + V_{H|\text{MoS}_2})$. Based on such information, we have found that the calculation results are almost similar regardless functional.

References for Supplementary Information

1. Ceperley, D. M.; Alder, B. J., Ground State of the Electron Gas by a Stochastic Method. *Physical Review Letters* **1980**, *45* (7), 566-569.
2. Grimme, S.; Ehrlich, S.; Goerigk, L., Effect of the damping function in dispersion corrected density functional theory. *J Comput Chem* **2011**, *32* (7), 1456-65.
3. Lee, K.; Murray, É. D.; Kong, L.; Lundqvist, B. I.; Langreth, D. C., Higher-accuracy van der Waals density functional. *Physical Review B* **2010**, *82* (8).
4. Guo, Y.; Robertson, J., Band engineering in transition metal dichalcogenides: Stacked versus lateral heterostructures. *Applied Physics Letters* **2016**, *108* (23).